Research Square

Preprints are preliminary reports that have not undergone peer review.
They should not be considered conclusive, used to inform clinical practice,
or referenced by the media as validated information.

Partially decoupling cell size and density as tailorable design parameters in mSLA-printed gyroid cores for sustainable sandwich panels

Lwazi Luthuli[1]
University of Cape Town
Samuel Schlesinger[1]
University of Cape Town
Mikael Christodoulides[1]
University of Cape Town
Maxwell Vos
University of Cape Town
Sherlyn Gabriel[1]
University of Cape Town
James A Dicks[1]
james.dicks@uct.ac.za

University of Cape Town

Research Article

Keywords: additive manufacturing, masked stereolithography, triply periodic minimal surface, gyroid, sandwich panel, lattice core, basalt fibre, biobased composites

Posted Date: November 12th, 2026

DOI: https://doi.org/10.21203/rs.3.rs-11455393/v1

License: This work is licensed under a Creative Commons Attribution 4.0 International License.
Read Full License

Additional Declarations: No competing interests reported.

Partially decoupling cell size and density as tailorable design parameters in mSLA-printed gyroid cores for sustainable sandwich panels

Lwazi Luthuli[1], Samuel Schlesinger[1], Mikael Christodoulides[1], Maxwell Vos[1], Sherlyn Gabriel[1, 2] and James A Dicks[1]*

[1]Centre for Materials Engineering, Department of Mechanical Engineering, University of Cape Town, South Africa

[2]Blast Impact Survivability Research Unit, Department of Mechanical Engineering, University of Cape Town, South Africa

*Corresponding author: james.dicks@uct.ac.za

Abstract

Lightweight sandwich cores can be tailored to the load case, yet design rules linking lattice architecture to core and panel performance are lacking for vat photopolymerisation. Sheet-network gyroid lattices were printed by masked stereolithography (mSLA) from a partially biobased PLA-based resin across a full factorial of unit cell size (5–20 mm) and nominal density (5–20%). The printable window, density, wall thickness and compressive properties were characterised. Selected cores were integrated into sandwich panels with basalt fibre facesheets in a partially biobased epoxy matrix and tested in flexure. Printability was bounded by wall separation below ≈130 μm and by resin entrapment in 5 mm cells at high density. Cell size controlled wall thickness (132–271 μm at 5% density), whilst apparent density was independent of cell size at low density ($p \geq 0.14$), so the two act as partially decoupled design levers. Compressive strength followed bending-dominated Gibson–Ashby scaling ($n \approx 1.5$ in the defect-free range and ≈2 across the full window). A cell-size effect on strength was robust at 20% density on raw and ρ^2-normalised bases, and emerging at 15%. It is attributed to coupled wall thickness and cell count rather than the architecture itself. Panel flexural rankings matched core rankings. The 20 mm/20% core yielded the stiffest panels whilst the 5 mm/10% core gave the most strain-tolerant, benignly failing panels. These results establish mSLA gyroid lattices as tailorable sandwich cores, provide indicative design rules for core selection, and show that partially biobased constituents can form structurally efficient sandwich panels.

Keywords: additive manufacturing; masked stereolithography; triply periodic minimal surface; gyroid; sandwich panel; lattice core; basalt fibre; biobased composites

1 Introduction

Lattice structures have become popular structural materials for lightweight applications, and the development of additive manufacturing (AM) technologies has made the fabrication of complex lattice geometries increasingly accessible.[1, 2] Whilst appreciable developments have been made for laser powder bed fusion fabrication of metallic lattices and fused filament fabrication (FFF) of polymeric lattices, vat photopolymerisation AM has remained comparatively underdeveloped in this context. Vat photopolymerisation typically uses liquid monomer systems (commonly termed "resins") to produce thermosetting materials in a layer-by-layer process, creating opportunities to use materials with high Young's modulus and strength for structural purposes when compared to thermoplastic filaments often used in FFF. Furthermore, the technology facilitates high detail resolution, with pixel resolutions in the tens of micrometres and below now commonly accessible on commercial printers, allowing thin and detailed features beyond the usual capabilities of FFF.[3, 4] Additionally, through careful parametric optimisation these technologies can largely suppress the print-orientation-induced anisotropy that is a ubiquitous shortcoming of extrusion-based technologies.[5, 6] Given these benefits, a growing number of studies have used stereolithography (SLA), digital light processing (DLP) and masked stereolithography (mSLA) to develop lattice structures, including strut-based lattices[7], orientation studies[6], soft polymeric devices [4] and triply periodic minimal surface (TPMS) architectures in compression[8, 9], tension[10] and novel polycontinuous variants[11].

Structurally, TPMS geometries are particularly interesting non-stochastic lattice architectures for engineering applications. TPMS structures are mathematically designed to minimise surface area whilst maintaining zero mean curvature, allowing a theoretically minimal amount of material to achieve a specific volume and yielding a smooth surface that is uniformly curved in all

directions.[12] Conformationally, TPMS structures exhibit three-dimensional periodicity and a smooth, non-intersecting topology, which effectively minimises stress concentrations. Two predominant methods exist for generating TPMS gyroid structures, namely the sheet-based method, which produces a double gyroid composed of two offset minimal surfaces, and the skeletal method, which treats one of the subdomains as a solid network. Sheet-based gyroids have repeatedly been shown to mechanically outperform their skeletal (ligament-based) counterparts under compression.[13]

Within vat photopolymerisation of TPMS lattices, prior work has largely concentrated on scaffold and biomedical applications[14-17], on surface quality[18], or on comparing architectures at fixed porosity[19-21]. However, a small selection of parametric studies has been performed. For example, gyroid lattices produced by LCD photopolymerisation have been explored across design parameters[13], thin-walled TPMS structures printed by mSLA have been characterised for heat exchangers[22], and SLA printed gyroids have been optimised with respect to print orientation, cell size, and wall thickness[23]. Most directly, the influence of cell size and wall thickness on the compressive behaviour has been systematically studied for gyroid structures using FFF of PLA, yet this AM technology's achievable wall thicknesses, surface quality and degree of anisotropy differ fundamentally from vat photopolymerisation.[24] Furthermore, the compressive behaviour of vat-printed strut and gyroid lattices across porosities and base materials has been mapped[25], and relationships between geometry and density for five SLA-printed TPMS architectures have been explored.[26] However, in both cases cell size and wall thickness co-varied with relative density, such that their independent effects cannot be separated. A decoupling approach has precedent in metallic lattices, where unit cell size and wall thickness were decoupled in laser powder bed fusion Ti–6Al–4V gyroids to establish representative volume element limits[27]. However, to the best of

our knowledge, an equivalent full-factorial treatment of mSLA sheet-gyroids, including the boundaries of the printable window, has not been reported.

At the application level, sandwich structures with additively manufactured cores have been widely studied for FFF-printed strut, honeycomb, corrugated and auxetic cores[28-31], including FFF-printed gyroid cores with carbon fibre laminate facesheets[32]. Importantly, photopolymer-based sandwich constructions also exist. For example, sandwich beams with strut-based cores printed from a photopolymer ceramic resin have been tested[33], DLP-printed fibre-reinforced sandwich beams with thermoset matrices have been manufactured[34], fabrication quality of sandwich structures with photopolymer-resin TPMS cores has been explored[35], and a gyroid building-block sandwich bridge deck has been developed[36]. These works establish the feasibility of vat photopolymerisation cores in sandwich construction. However, because they treat single core designs or compare topologies, they do not systematically account for how the two primary core design parameters, namely unit cell size and wall thickness, independently shape core properties within the printable window, and whether those core-level effects carry through to panel-level response. Designers of resin-AM sandwich cores therefore have little empirical guidance on which design parameter to adjust.

Constituent selection also governs the sustainability of such panels. Most commercial photopolymer resins and laminating epoxies are derived from petrochemical feedstocks, and sandwich facesheets are typically made from energy-intensive glass or carbon fibre.[37, 38] Biobased photopolymer resins, in which part of the oligomer or monomer content is derived from renewable feedstocks such as lactic acid or plant oils, are now commercially available for vat photopolymerisation. However, they have mainly been applied to decorative, dental and biomedical parts, and their use in load-bearing lattices remains largely unexplored. Lattice cores

also offer an inherent resource benefit, since material is placed only where it carries load, and tuning cell size and density allows the resin mass to be minimised for a given performance target. Pairing biobased lattice cores with low-impact mineral fibre facesheets such as basalt and partially biobased matrices therefore offers a route to sandwich panels with reduced reliance on fossil-derived constituents, provided that their mechanical performance can be designed with confidence.[39-41]

This study therefore aims to ascertain whether unit cell size and wall thickness can be used as (partially) independent design levers for mSLA-printed sheet-gyroid sandwich cores, and whether core-level trends are consistent with panel-level flexural response. Using a commercial, partially biobased PLA-based photopolymer resin, we (i) map the printable window of sheet-gyroid lattices across a 4×4 factorial of unit cell size and nominal relative density, (ii) quantify the fidelity between nominal and measured density and wall thickness, (iii) establish compressive structure–property relationships including Gibson–Ashby scaling exponents, and (iv) demonstrate panel-level flexural behaviour for four selected cores integrated into sandwich panels with basalt fibre facesheets and a partially biobased epoxy matrix.

2 Experimental

2.1 Materials

eSun eResin-PLA Pro transparent resin (eSun, China, purchased from DIYElectronics, South Africa) was used as received. According to the manufacturer, the resin is formulated from a polyurethane acrylate oligomer (PLA-PUA) synthesised from a biobased polylactic acid diol, which is derived mainly from corn starch. The biobased carbon content of the formulated resin is

not disclosed, so the resin is described here as partially biobased, and no quantitative life cycle claims are made for it. Propan-2-ol (isopropyl alcohol, 99%, Kimix Chemicals, South Africa) was used for washing. Woven basalt fabric (plain weave, areal density 205 g/m², thickness 0.2 mm, Colan, Australia) was used as received for the sandwich panel facesheets. Gurit BioPrime37 (37 wt% renewable content) and Ampreg 3X slow hardener (purchased from AMT Composites, South Africa) were used as received for the facesheet matrix.

2.2 Lattice design

Sheet-network Schoen gyroid lattices were designed using the open-source MSLattice software (MATLAB-based[12]). In the sheet-network approach, the minimal surface is offset in both normal directions such that a double surface is formed, and the solid domain is the region bounded by the two offset surfaces, according to Equation 1.

$$-c \leq \phi(x, y, z) \leq c \qquad \text{Equation 1}$$

where φ(x, y, z) is the level-set function of the Schoen gyroid, according to Equation 2.

$$\phi(x, y, z) = \sin X \cos Y + \sin Y \cos Z + \sin Z \cos X \qquad \text{Equation 2}$$

where X = 2παx, Y = 2πβy, Z = 2πγz, α, β and γ being constants related to the unit cell size, and x, y and z the spatial directions. The iso-value c therefore sets the wall thickness directly. At c = 0 the surface divides the volume equally, and increasing |c| thickens the solid domain, raising the nominal relative density at fixed cell size.

A full factorial design of unit cell size (5, 10, 15 and 20 mm) and nominal density (5, 10, 15 and 20%) was adopted (Table 1). Nominal densities were converted to nominal apparent densities using the solid resin density (1.10 g/cm³), giving 55, 110, 165 and 220 kg/m³. Both conventions

are reported throughout for clarity. Compression specimens were designed as 30 mm cubes. Panel cores were designed at 200×75×30 mm^3. A thin (200 μm) solid sheet was added to the top and bottom faces of the lattice CAD, to avoid resin penetration during sandwich panel construction and improve interfacial adhesion of the core and facesheets. Pilot printing of 2 mm unit cells (20–30% nominal density) produced solid blocks owing to resin entrapment and informed the lower cell-size bound of the factorial.

Table 1. Full-factorial experimental matrix of sheet-gyroid lattice parameters, with specimen nomenclature (cell size–nominal density, e.g., 10-15).

Unit cell size (mm)	55 kg/m³ (5%)	110 kg/m³ (10%)	165 kg/m³ (15%)	220 kg/m³ (20%)
5	5-5	5-10	5-15	5-20
10	10-5	10-10	10-15	10-20
15	15-5	15-10	15-15	15-20
20	20-5	20-10	20-15	20-20

2.3 Additive manufacturing

Printing was performed on a masked stereolithography printer (GK III Ultra, Uniformation, Taiwan) fitted with a removable spring-steel build platform. A layer height of 25 μm, lift speed of 45 mm/min and retract speed of 60 mm/min were used. The normal layer cure time of 3.6 s was determined from a Jacobs working curve[42] following our previous optimisation of this resin using mSLA 3D printing.[4, 5] STL files were sliced in CHITUBOX, and six specimens per build were arranged in two rows of three on the virtual build plate. After printing, specimens were washed in isopropyl alcohol in an ultrasonic bath to remove excess resin, dried, and post-cured in a UV chamber (UW-02, Creality, China, 365–385 nm) for 15 min. Cured specimens were stored in closed containers with tissue interleaves to prevent handling damage.

2.4 Sandwich panel fabrication

Sandwich panels were manufactured by a hand lay-up. Woven basalt fabric was impregnated with a resin mixture of BioPrime37 and Ampreg 3X (100:29 wt ratio) and laid onto the top and bottom faces of the printed lattice cores. The assembled panels were placed between layers of breather fabric and peel ply on each side and consolidated under mechanical pressing at ambient temperature for 18 h, followed by postcuring at 50 °C for 16 h. Final panel dimensions were approximately 200×75×31 mm^3.

2.5 Characterisation and mechanical testing

Apparent density was measured from specimen dimensions using digital calipers (InSize, resolution of 0.01 mm) and mass (Mettler Toledo, resolution of 0.00001 g). Wall thickness was measured by optical microscopy (Nikon SMZ25 stereo microscope, Nikon, Japan) with NIS-Elements Imaging software from five measurements on one specimen per condition, reported as mean ± standard deviation.

Uniaxial compression testing of the 30 mm cube cores was performed according to ASTM C365 on a universal testing machine equipped with a 10 kN loadcell (Zwick 1484, Germany) at a crosshead speed of 5 mm/min, compressed along the build direction. Specimen displacement was tracked using an integrated video extensometer (LIMESS, Germany). The compressive modulus (E_c) was taken from the slope of the linear elastic region of the stress–strain curve, and the ultimate compressive strength (UCS) as the first peak stress. Three specimens per condition were tested unless otherwise noted. Results are reported as mean ± standard deviation.

Flexural testing of sandwich panels was performed according to ASTM C393 (beam flexure) on a universal testing machine equipped with a 10 kN loadcell (Zwick 1484, Germany) at a crosshead

speed of 6 mm/min, with a support span of 150 mm and two loading points at the third-span positions, 50 mm apart. This four-point configuration was adopted from comparable sandwich studies[43, 44] because ASTM C393 does not prescribe a fixed span for such cores. Because C393 is fundamentally a core-shear test and the present panels had span-to-thickness ratio ≈5 with comparatively compliant cores, load–deflection data were reduced using the homogeneous beam approximation. The resulting quantities are therefore reported as apparent flexural modulus (E_f) and apparent flexural strength (FS) and should be read as comparative design metrics rather than standard ASTM C393 characteristic properties.

Specific properties are defined throughout as the property divided by the relevant measured apparent density, according to Equation 3.

$$\text{specific property} = \frac{\text{property}}{\rho_{\text{app}}} \qquad \text{Equation 3}$$

where ρ_{app} is the measured core density for core-level properties and the measured whole-panel density (including facesheets) for panel-level properties. The two bases are never intermixed.

Gibson–Ashby scaling analysis was performed by log–log linear regression of compressive strength and modulus against measured relative density (measured apparent density normalised by the solid resin density, 1.10 g/cm³) for each unit cell size, using Equation 4.

$$\frac{\sigma}{\sigma_s} = C\left(\frac{\rho}{\rho_s}\right)^n \qquad \text{Equation 4}$$

where, for the modulus, n ≈ 1 indicates stretch-dominated and n ≈ 2 bending-dominated behaviour, the corresponding strength exponents being n ≈1 and n ≈1.5, respectively.[45]

Statistical comparisons used one-way ANOVA across cell sizes within each nominal density level, with Welch's two-sample t-tests (unequal variances) for pairwise comparisons, with significance taken at $p < 0.05$. Analyses used the per-specimen data ($n = 3$ per condition, $k = 12$ points per cell size in the scaling fits). Within-level comparisons spanned the 10, 15 and 20 mm cell sizes unless stated otherwise. The 5 mm conditions were excluded from these tests as a degraded-fidelity processing zone (Section 3.3). Density-controlled comparisons additionally used per-specimen, per-level analysis of covariance of log strength on cell size with log measured density as covariate. Ratio normalisations (specific strength and strength normalised by ρ^2) were reported as sensitivity analyses, and the sensitivity of the ρ^2 basis to the normalisation exponent was checked over $n = 1.5–2.3$. The ρ^2 basis was adopted as a conservative upper bound on the density scaling rather than as an assumed constitutive exponent. At the defect-free strength exponent identified in Section 3.4 ($n \approx 1.5$), the 20% contrasts strengthen relative to this basis, with the 10 vs 15 mm Welch test moving from $p = 0.049$ to $p = 0.025$ (Table S4). A common-slope analysis of covariance of log strength against log relative density across the 10, 15 and 20 mm series ($k = 36$) tested whether the cell-size effect on strength takes the form of a uniform prefactor shift across the printable window, with the interaction between cell size and log relative density tested first to justify the common-slope model (Figure S1). The analysis basis, inclusion sets, full within-level results, scaling fits, and normalisation sensitivity are given in the SI (Tables S1 to S4).

3 Results and discussion

3.1 Printability window of gyroid lattices across cell size and density

Despite mSLA printers offering pixel resolutions below 20 μm, other physical limitations constrain the minimum feasible feature size and detail fidelity that can be achieved. Furthermore,

factors such as polymerisation shrinkage and residual monomer on the printed surface can cause discrepancies between nominal and printed geometries. Therefore, the attainable lattice cell sizes and wall thicknesses (varied through nominal relative density) were investigated first. Two boundaries of the printable window were identified (Figure 1). At the lower bound, 5-5 lattices failed to print because the thin walls (nominally below ~130 µm) could not withstand the separation forces during layer lifting. This is consistent with Stefan adhesion, the suction force generated as the cured layer is peeled from the vat film. This force exceeded the strength of the incompletely cured lattice and destroyed the object during printing. A related but less severe manifestation was observed in the thinnest successfully printed walls (e.g., 10-5, measured wall thickness 132 ± 3 µm), where randomly distributed pores formed in the walls (Figure 1b). Since the printer builds parts in an inverted orientation, portions of solidifying material can fail to remain connected to the bulk of the lattice. These defects plausibly explain the larger experimental scatter observed for thin-walled conditions as discussed later.

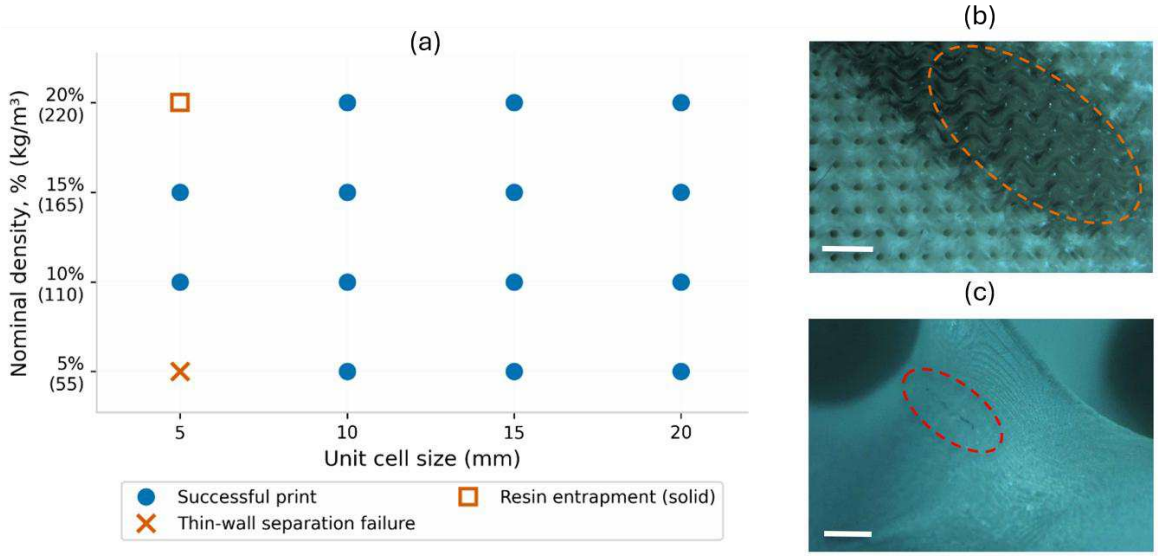


Figure 1. a) Printable window map of sheet-gyroid lattices over unit cell size (x-axis, mm) and nominal relative density (y-axis, %), and optical micrographs of b) resin entrapment (scale bar 3 mm), c) pore defect (scale bar 500 µm).

At the upper bound, 5-20 lattices did not produce open lattice structures. Although solid objects printed, the internal regions became homogeneous solids. This was attributed to a combination of light bleed/overcure into narrow pore channels and the inability to wash uncured resin out of the narrow channels. The same mechanism turned the pilot 2 mm cell structures (20–30% density) into solid blocks.[46, 47] All other unit cell sizes (10, 15 and 20 mm) printed successfully over the full nominal density range (55–220 kg/m³). It should be emphasised that both window boundaries are specific to this resin–printer–exposure combination. The ~130 μm separation-failure threshold in particular is expected to shift with exposure dose, vat-film adhesion and resin green strength, and should be read as a process parameter rather than a material constant. Nevertheless, layer cure time was selected based on prior parametric optimisation for mechanical properties and thus this effect was not further explored.[48] Additionally, these wall thicknesses are some of the thinnest examples reported in recent literature, highlighting the efficacy of mSLA 3D printing to achieve low density porous structures.[47, 49-54]

3.2 Printing fidelity relative to measured density and wall thickness

Two fidelity observations emerged when comparing the measured apparent density and wall thickness for all printed conditions (Table S5 and Figure 2). Firstly, measured densities were consistently higher than nominal. The excess was 9.9–18.0% at 5%, 14.6–16.4% at 10%, 12.7–22.0% at 15% and 14.6–21.1% at 20% nominal density, roughly 10–22% across the range with no systematic density trend. This pattern is inconsistent with a uniform overcure offset as the primary cause. A constant per-wall overcure increment would add a roughly fixed thickness, so the relative density excess should shrink ~1/t as walls thicken, which is not observed. Moreover, at 5% nominal density the measured walls are 12–18% thinner than the first-order nominal estimate ($t \approx \rho L/3.09$ from the gyroid surface area), whilst the measured density is 10–18% above nominal, so the

surplus mass does not appear to reside in the walls as measured. A plausible contributor is residual resin retained at nodes and in narrow channels after washing, resulting in additional solids deposited on the surfaces after postcuring.[21, 46, 47] Secondly, and central to this study, the dependence on unit cell size differed between the two quantities. Measured apparent density did not differ significantly across cell sizes at 5% (one-way ANOVA, $p = 0.14$) or 10% ($p = 0.70$) nominal density, but did differ at 15% ($p = 0.027$, with 15-20 highest at 266.3 kg/m³) and 20% ($p = 0.032$).

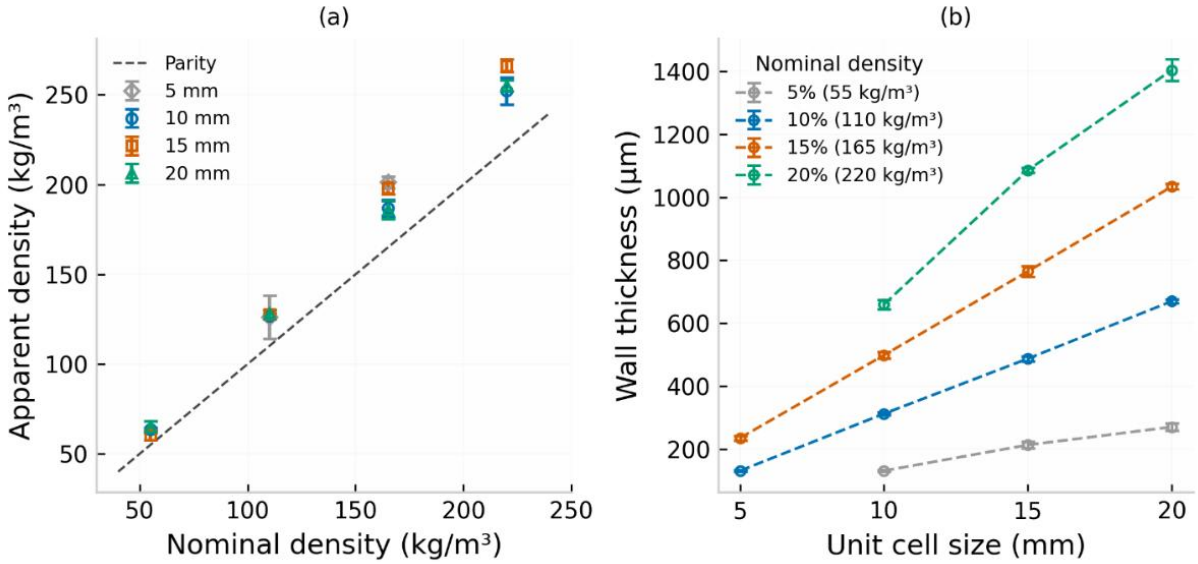


Figure 2. (a) Nominal vs measured apparent density for all printed conditions (symbols show cell size, dashed line shows parity), and (b) Measured wall thickness vs unit cell size for each nominal density level.

From these results, the low-density null result requires qualification. The max–min spread of condition means was 7% of the grand mean at 5% and only 1% at 10%, and with $n = 3$ per condition the pairwise minimum detectable effect at 80% power was ≈12% and ≈5% of the mean, respectively. The low-density claim is therefore one of no detectable cell-size dependence at this sample size, with the true effect bounded to a few per cent, rather than proven invariance. In

contrast, measured wall thickness increased strongly and monotonically with unit cell size at every density level, from 132 ± 3 μm (10-5) through 214 ± 10 μm (15-5) to 271 ± 11 μm (20-5), because the iso-value offset applied over a larger unit cell produces a proportionally thicker gyroid sheet. Unit cell size and wall thickness are therefore partially decoupled design parameters. At low density they are effectively independent, whilst at high density a residual cell-size effect on density (≤8%) accompanies the dominant thickness effect.

3.3 Compressive properties of the lattice cores

Representative compressive stress–strain curves exhibited the expected sequence for cellular solids (Figure 3), namely a linear elastic region, a peak stress (taken as the UCS), and a stepwise softening regime associated with progressive microcracking and wall fragmentation, as previously described for similar lattice structures.[22] Progressive testing towards densification was not performed since brittle fracture of the lattice structures typically occurred prior to this regime. The full-factorial compressive properties are presented in Table S6.

The cell-size effect on strength was strongly conditional on density. At 5% and 10% nominal density, UCS did not differ significantly across the 10, 15 and 20 mm cell sizes ($p = 0.55$ and $p = 0.34$, respectively). Including the degraded 5-10 condition at the 10% level made that test significant ($p = 0.0025$), owing to its defects. At these wall thicknesses (132–313 μm) the defect population described previously plausibly dominates over any geometric size effect. At higher densities, however, the effect emerged. At 15%, UCS differed across cell sizes ($p = 0.034$), with the 20 mm condition exceeding the 10 mm condition (Welch's t-test, $p = 0.022$), whilst the 20 vs 15 mm contrast did not reach significance on the raw basis ($p = 0.074$). The ordering at this level was non-monotonic (20 > 10 > 15 mm), so the 15% effect is specifically a 20 mm advantage rather

than a smooth size gradient. At 20%, the effect was even more pronounced ($p < 0.0001$), with UCS rising from 3.10 ± 0.07 MPa (10 mm) to 4.10 ± 0.06 MPa (15 mm, $p = 0.0001$) and 4.06 ± 0.08 MPa (20 mm, $p = 0.0001$ vs 10 mm), whilst the 15 and 20 mm conditions were statistically indistinguishable from each other ($p = 0.44$).

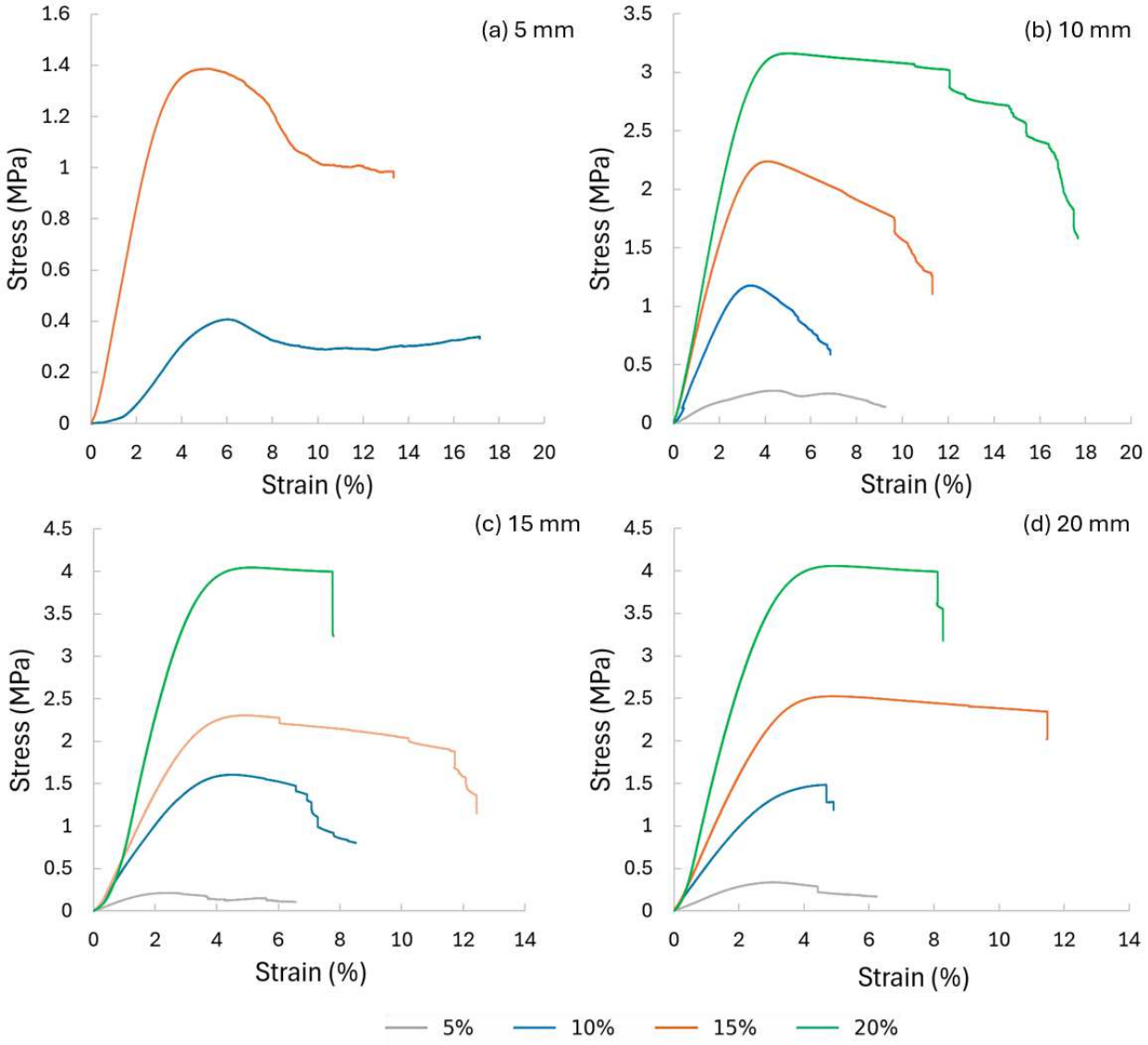


Figure 3. Representative compressive stress–strain curves for each cell size at 15% nominal density (10, 15, 20 mm, and 5-15 additionally).

Because measured density itself differed across cell sizes at these two levels (Section 3.2), the comparison was repeated on per-specimen specific strength (UCS/measured density) to separate

the cell-size effect from the density surplus. The cell-size effect persisted after this normalisation. At 15% nominal density, specific strength differed across cell sizes (ANOVA, $p = 0.030$), with the 20 mm condition exceeding the 15 mm condition ($p = 0.032$). At 20%, the effect remained pronounced ($p = 0.0001$), with the 10 mm condition (0.01231 ± 0.00060 MPa·m³/kg) falling below both the 15 mm (0.01541 ± 0.00005, $p = 0.012$) and 20 mm (0.01590 ± 0.00041, $p = 0.0018$) conditions, which did not differ from each other ($p = 0.17$). Since strength scales approximately with the square of density ($n \approx 2$, Section 3.4), division by ρ removes only a linear density dependence, and the denser conditions retain a residual advantage in this comparison. The test was therefore repeated with strength normalised by ρ^2. The effect persisted on this stricter basis. At 15% nominal density the across-size difference remained significant (ANOVA, $p = 0.030$), with the 20 mm condition exceeding the 15 mm condition ($p = 0.022$). At 20% the effect remained pronounced (ANOVA, $p = 0.0018$), with the 10 mm condition falling below both the 15 mm ($p = 0.049$) and 20 mm ($p = 0.011$) conditions, whilst the 15 and 20 mm conditions remained statistically indistinguishable ($p = 0.063$). As a primary, regression-based density control, per-specimen analysis of covariance of log strength with log measured density as covariate returned $p = 4.6 \times 10^{-5}$ at 20% but $p = 0.12$ at 15%. The ratio-normalised conclusions were unchanged for normalisation exponents between 1.5 and 2.3, except for the 10 vs 15 mm contrast at 20%, which became marginal above $n \approx 2.1$. The 20% cell-size effect therefore survives density control on every basis and is not a density artefact. The 15% effect, by contrast, depends on the method used and is therefore regarded as emerging rather than established. However, the gyroid is self-similar at fixed relative density. Within a fixed specimen volume, changing the cell size therefore also changes the absolute wall thickness and cell count, so a pure cell-size effect cannot be isolated in this design. The observed effect is therefore one of absolute wall thickness and/or

cell count rather than architecture in the strict sense. Cell size is retained as shorthand for this coupled variation.

The E_c followed the same pattern as UCS. At 20% density, the 20 mm condition (161.3 ± 4.0 MPa) exceeded both the 10 mm (101.0 ± 3.6 MPa, $p < 0.0001$) and 15 mm (106.2 ± 10.7 MPa, $p = 0.007$) conditions, the latter of which did not differ from each other ($p = 0.50$). The strain at UCS was confined to ≈3–5% for all conditions (Table S6), indicating that the deformation mode up to peak load was architecture-invariant. One qualification applies to the inferential results in this section. The p-values are reported uncorrected, and across the approximately 26 tests reported, the marginal 15% results ($p = 0.030$–0.034) do not survive a per-level Holm correction, whilst the 20% effects ($p \leq 0.0018$ on the raw, specific and ρ^2-normalised bases) do. The cell-size effect on strength should accordingly be read as robust at 20% and emerging at 15%.

The two printable 5 mm conditions warrant explicit discussion, since they depart from the trends described above. The 5-10 and 10-5 lattices share the same measured wall thickness (132 ± 3 μm). This is expected from the geometry, since sheet thickness scales with the product of density and cell size ($t \propto \rho L$), giving both conditions the same nominal thickness. At matched wall thickness, and with strength normalised by ρ^2, 5-10 reaches only ≈46% of 10-5 and 5-15 only ≈61% of 15-5, so thin walls alone cannot explain the deficit. The cell-count argument also cuts the other way here, since the 5 mm cubes contain the most cells of any condition (6 per edge) and boundary effects should, if anything, favour them. The deficit is instead attributed to a small-channel processing effect involving partial resin entrapment, cure broadening into the narrow channels and incomplete washing. This is the same mechanism that rendered 5-20 solid, acting partially at 5-10 and 5-15. The unusually large scatter in the 5-10 density (±12.0 kg/m³, against ≤ ±7.5 kg/m³ for all other conditions) and modulus (5.8 ± 3.8 MPa) supports this interpretation. In this framing, the

5 mm cells occupy a degraded-fidelity zone within the printable window, rather than failing only at its 5-20 boundary.

3.4 Scaling behaviour and the decoupling of cell size from density

Gibson–Ashby scaling was fitted to the per-specimen properties against measured relative density for each cell size to place the density dependence quantitatively (Figure 4). Strength exponents were statistically indistinguishable across cell sizes, at n = 1.92 (95% CI 1.71–2.12), 2.00 (1.69–2.31) and 2.02 (1.77–2.28) for the 10, 15 and 20 mm cells (R^2 = 0.95–0.98). However, the log–log relationship is significantly curved (quadratic test on the pooled fit, $p = 1.8 \times 10^{-5}$). Excluding the defect-prone 5% conditions, the common strength exponent drops to n ≈ 1.5 (modulus n ≈ 1.3), matching the classic bending-dominated collapse-strength prediction. The steeper full-window exponent therefore reflects the systematic weakness of the thinnest, defect-bearing walls rather than the intrinsic architectural scaling. This provides independent evidence for the defect-dominance interpretation of Sections 3.1 and 3.3. The full-window values nonetheless agree with those reported for sheet gyroids produced by other AM processes.[24, 55] Modulus exponents were, however, lower with n = 1.50 (95% CI 1.32–1.68) and 1.55 (1.22–1.89) for the 10 and 15 mm cells, rising to 1.89 (1.68–2.11) for the 20 mm cells. The pooled fits across the three fitted cell sizes gave n = 1.98 (R^2 = 0.96) for strength and n = 1.64 (R^2 = 0.94) for modulus. The pooled modulus exponent sits between the per-cell-size values, reflecting the cell-size dependence of the modulus prefactor. The consistency of the strength exponent across cell sizes demonstrates that density scaling is architecture-invariant within the printable window. Cell size instead changes the prefactor, through wall thickness and its associated defect population, rather than the scaling physics.

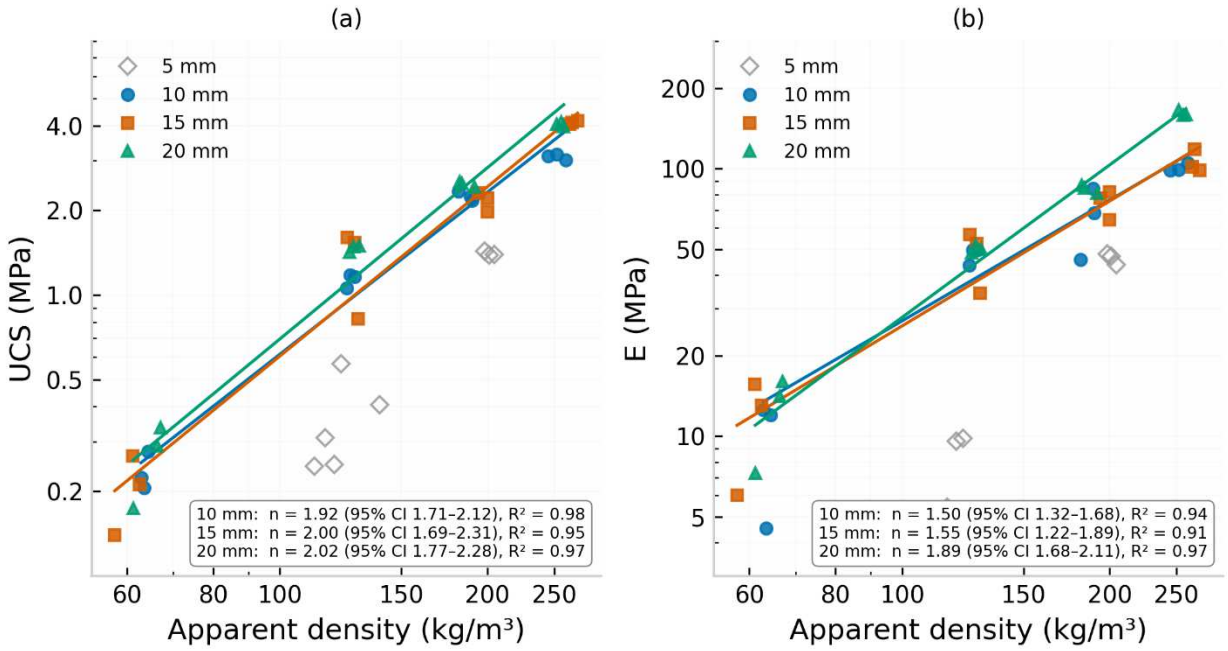


Figure 4. Log–log Gibson–Ashby scaling of (a) UCS and (b) compressive modulus against measured relative density, per cell size. Individual specimens are plotted (n = 3 per condition) and fit lines correspond to the 10, 15 and 20 mm series.

A common-slope (ANCOVA-type) fit of log strength against log relative density across the 10, 15 and 20 mm series returned a shared exponent of n = 1.98 with no significant cell-size main effect on the prefactor ($p = 0.13$). This indicates that the cell-size effect on strength is conditional on density and emerges only at 15–20% nominal density, rather than acting as a uniform prefactor shift across the window. At $k = 36$, however, the interaction and main-effect tests have limited power against an effect concentrated at the highest density level, where the log-spacing compresses the predictor range. The within-level tests of Section 3.3 exploit replication at that level and are therefore more sensitive to this effect. The non-significant ANCOVA terms should not be read as evidence that the effect is absent. Note that the fits are density normalised by the solid resin density only. Bulk compressive properties of the cured resin were not measured, so the prefactor C is not interpreted in absolute terms, and the exponents are the transferable quantities.

Expressed in terms of specific properties, the consequence for design is direct. At 20% nominal density, specific strength increased from 0.0123 MPa·m³/kg (10 mm) to 0.0154 MPa·m³/kg (15 mm), and 0.0159 MPa·m³/kg (20 mm), whereas at 5% density specific strength was flat within scatter (0.0032–0.0041 MPa·m³/kg). This indicates that once walls are thick enough to print defect-free, larger cells deliver thicker, stronger walls at the same mass. It is worth noting that this direction contrasts with FFF gyroid studies, in which smaller cells for ABS gyroids were recommended and an increase in specific compressive strength with decreasing cell size has been found.[56] A plausible reconciliation lies in the process differences that occur between FFF and layer-by-layer vat photopolymerisation AM. In FFF the number of inter-bead interfaces multiplies as cells shrink at fixed overall dimensions, introducing defect populations that scale inversely with cell size. The vat-cured walls here are continuous, and the iso-value offset gives larger cells proportionally thicker walls at matched nominal density. The cell-size effect is therefore process-dependent, and the present conclusion is bounded accordingly.[56, 57] The present regime of 130–300 μm walls at densities below 130 kg/m³ is largely inaccessible to FFF, where nozzle diameter and inter-bead bonding constrain gyroid walls to appreciably larger thicknesses.[24, 27]

3.5 Sandwich panel flexural response

Four cores spanning the design space were selected for panel integration to explore whether core-level rankings transferred to the panel level. Here, 20-20 (highest stiffness/strength), 10-15 (intermediate), 10-5 (lowest density) and 5-10 (thin-walled, most strain-tolerant) were chosen. Panels were tested in four-point beam flexure per ASTM C393. Given the compliant cores and span-to-thickness ratio, results are reported as apparent flexural properties for comparative purposes. The four designs were chosen to span the performance envelope rather than to separate the two core parameters. The only pair sharing a parameter is 10-5/10-15 (fixed cell size, varied

density), and no fixed-density pair was tested, so the panel data cannot isolate a cell-size effect from a density effect. Representative flexural stress–strain curves are shown in Figure 5, and characteristic flexural properties are presented in Table 2.

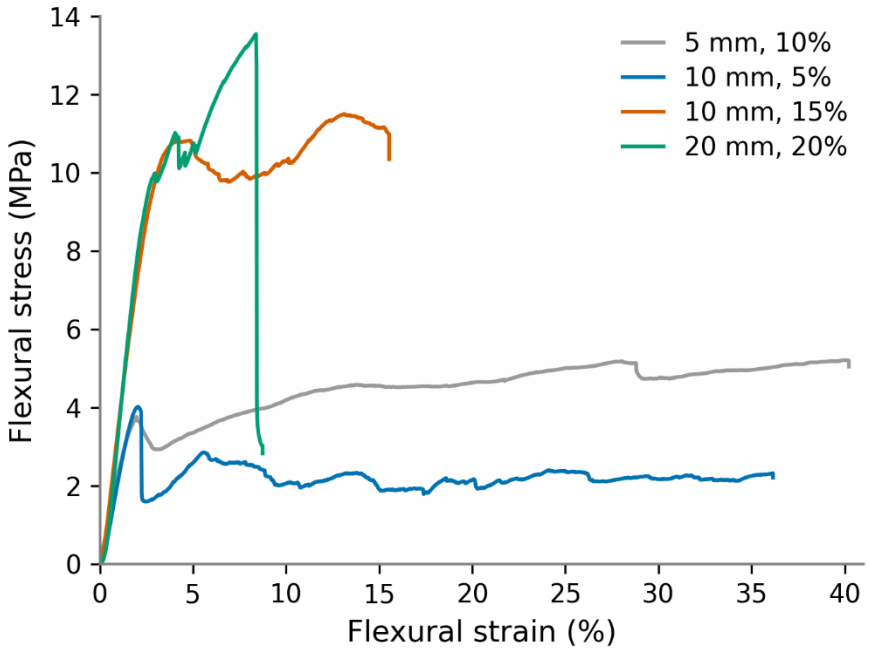


Figure 5. Representative flexural stress-strain curves for the four panel designs. Curves correspond to specimen 3 for the 5-10, 10-5 and 10-15 panels and specimen 2 for the 20-20 panel.

Panel apparent densities ranged from 169 ± 6 kg/m³ (10-5 core) to 327.2 ± 0.1 kg/m³ (20-20 core) (Table 2). The surplus of panel over core density was ≈155 kg/m³ for the 5-10 design, against ≈70–105 kg/m³ for the other three designs. This may indicate resin ingress into the small cells during lay-up, which is directly relevant to the benign failure of that panel. Nevertheless, the panel-level rankings were consistent with the core-level trends. The 20-20 panel achieved the highest specific apparent flexural modulus ($E_{f\ spec}$) (1.561 MPa·m³/kg) and specific apparent flexural strength (FS_{spec}) (0.042 MPa·m³/kg), followed closely by the 10-15 panel (1.539 MPa·m³/kg). Conversely, the 5-10 panel exhibited the lowest stiffness (0.766 MPa·m³/kg) but the greatest strain tolerance, consistent with the minimal, non-catastrophic failure observed for small-cell cores, in contrast to

the rapid failure of the 20-20 panels (Figure 6). The failure modes differed across the four designs, consistent with the differing curve shapes in Figure 5, and this difference is physically meaningful. However, because cell size and density varied together across the designs, the change in failure mode cannot be attributed to either parameter alone.

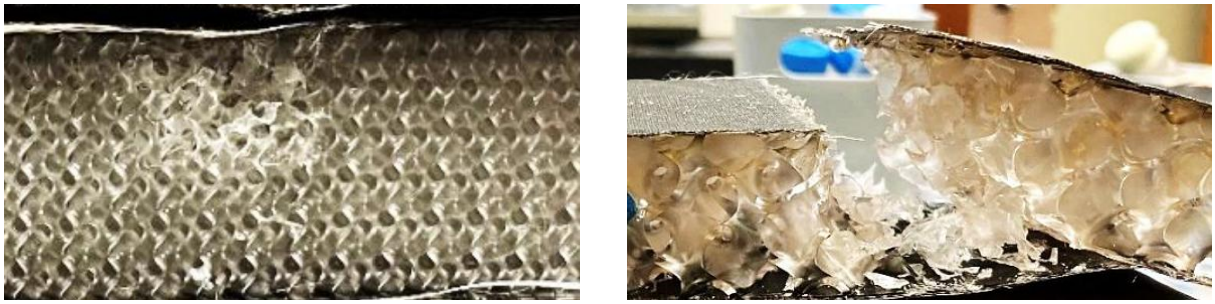


Figure 6. Photographs of failed panels showing the failure-extreme spectrum from minimal (5-10) to catastrophic (20-20).

It is worth noting that these four designs at one facesheet construction constitute a demonstration of consistency between core- and panel-level rankings, not a validated predictive transfer rule, and generalisation beyond the tested window is not claimed. Nonetheless, the twofold spread in $E_{f\,spec}$ across the four designs (0.77 vs 1.56 MPa·m³/kg), despite identical facesheets, shows that the panels were core-sensitive and that the facesheets did not dominate the core contribution. At the same time, the core modulus differs ≈2.2-fold between the 20-20 and 10-15 designs whilst the apparent panel modulus differs only ≈1.08-fold, which suggests that at high core stiffness the panel response becomes facesheet- or shear-limited.

Table 2. Sandwich panel flexural results.

Panel	ρ_{panel} (kg/m³)	E_f (MPa)	$E_{f\,spec}$ (MPa·m³/kg)	FS (MPa)	FS_{spec} (MPa·m³/kg)
5-10	281.5 ± 15.7	219 ± 7	0.77 ± 0.02	5.5 ± 0.4	0.02 ± 0.001
10-5	169.2 ± 5.8	262 ± 1	1.48 ± 0.04	4.2 ± 0.4	0.024 ± 0.002
10-15	290.0 ± 7.8	461 ± 1	1.54 ± 0.03	11.5 ± 0.1	0.040 ± 0.0007
20-20	327.2 ± 0.1	497 ± 14	1.56 ± 0.04	13.7 ± 1.5	0.042 ± 0.004

Beyond the core architecture, basalt fibre was selected for the facesheets because it offers a favourable balance between environmental impact and mechanical performance compared with conventional reinforcements. Basalt fibre is melt spun directly from crushed volcanic rock at approximately 1450 °C without additives, giving an embodied energy of approximately 16 MJ/kg and a CO_2 footprint of 0.4–0.67 kg CO_2-eq/kg.[58, 59] By comparison, glass fibre requires 30–40 MJ/kg (0.8–2 kg CO_2-eq/kg)[58-60] and Kevlar 257 MJ/kg (15–28.4 kg CO_2-eq/kg)[61-63], whilst basalt's consumptive and pollutive water use (≈0.75 l/kg) is orders of magnitude below that of plant fibres such as flax (≈920 l/kg)[40, 64]. Although basalt is not renewable per se, it is abundant and readily accessible, and its inorganic composition gives it higher mechanical properties and lower hygroscopicity than plant-based fibres.[59, 65] In prior work, plain-weave basalt fabric from the same supplier and the same partially biobased epoxy matrix gave the highest flexural modulus (42.4 ± 1.4 GPa) and flexural strength (353.9 ± 13.9 MPa) of the reinforcements tested, exceeding equivalent glass and Kevlar laminates.[66] Basalt therefore provides a lower-impact facesheet without sacrificing the facesheet stiffness needed to carry bending loads. Combined with the partially biobased photopolymer resin and epoxy matrix, the sandwich panels show that constituents can be chosen to reduce environmental impact without necessarily sacrificing mechanical performance.

3.6 Design implications and limitations

Taken together, the core and sandwich panel results yield a set of indicative design rules for mSLA gyroid sandwich cores, bounded by the tested window. Firstly, walls below ~130 μm risk separation failure and pore defects, and cells at or below 5 mm cannot be cleared of resin at high density. Secondly, relative density may be used as the primary lever for strength ($n \approx 2$ scaling). Cell size acts as a secondary lever once walls exceed the defect-dominated regime, and is robust

at 20% nominal density (surviving multiple-comparison correction) and emerging at 15%. Thirdly, core-level rankings are consistent with panel flexural rankings, with small-cell thin-walled cores trading stiffness for strain tolerance and failure benignity. However, this depends on the facesheet lay-up, which for a given material sets the stiffness of the facesheets relative to the core, and hence the homogeneity of the flexural response. Nevertheless, relative to FFF gyroid cores[24] and FFF gyroid-core sandwich panels[32], the mSLA route accessed wall thicknesses down to ≈130 μm and low apparent densities using thermosetting polymers that facilitate mechanical properties relevant to structural applications. Relative to prior vat photopolymerisation sandwich demonstrations[33-36], the present work adds the parameter-resolved core characterisation that those demonstrations did not attempt. The design rules also carry a resource benefit. Because larger cells deliver higher specific strength once walls are thick enough to print defect-free, a target core strength can be met at a lower density, and therefore with less resin.

Several limitations to this study must be acknowledged. Firstly, cell size and cell count co-vary, and free-boundary effects are known to influence gyroid properties at low cell counts.[27] The cell-size effects reported here at 15–20% density should therefore be read as combined size-and-count effects within this envelope, and the panel-level trends cannot resolve this confound, since the panel cores differed in cell size and density simultaneously (Section 3.5). Secondly, a single commercial resin and a single printer were used, and resin-dependent effects on thin-walled TPMS performance are known to be appreciable.[22] Thirdly, quasi-static loading only was studied here, and the dynamic response of these gyroids carries its own thickness dependence.[67] Fourthly, the environmental benefits of the panels are argued from constituent selection and literature data rather than measured directly. A cradle-to-gate life cycle assessment of the cores and panels, including resin washing, post-curing and end-of-life options for the thermoset constituents, is needed to

quantify them. These limitations bound the generality of the findings but do not alter them within the tested window.

4 Conclusions

This study set out to ascertain whether unit cell size and wall thickness can serve as (partially) independent design levers for mSLA-printed sheet-gyroid sandwich cores, and whether core-level trends are consistent with panel-level response. This goal was achieved through a full-factorial experimental design spanning cell sizes of 5–20 mm and nominal relative densities of 5–20%, coupled to flexural testing of sandwich panels with basalt fibre facesheets and a partially biobased epoxy matrix. Specifically,

a) The printable window was mapped. Thin-wall separation failure bounded the window below approximately 130 µm walls, resin entrapment bounded small (≤5 mm) cells at high density, and pore defects in thin walls increased experimental scatter.

b) Measured apparent density showed no detectable cell-size dependence at 5–10% nominal density but differed significantly at 15–20%, whilst wall thickness scaled strongly with cell size at all densities, partially decoupling the two parameters.

c) Compressive strength followed Gibson–Ashby scaling consistent with bending-dominated collapse (strength n ≈ 1.9–2.0 across the full window, n ≈1.5 in the defect-free 10–20% range, and modulus n ≈ 1.5–1.9). A cell-size effect on strength emerged where walls were thick enough to avoid defect dominance. It was robust at 20% nominal density, surviving multiple-comparison correction on the raw and ρ^2-normalised bases, and emerging at 15%. Given the self-similar lattice design, this effect is attributed to the coupled absolute wall thickness and cell count rather than to the architecture per se.

d) Panel flexural rankings were consistent with core-level rankings for the four tested designs. The 20-20 core gave the stiffest panels and the 5-10 core the most strain-tolerant and

benignly failing panels, bracketing the available trade-off between stiffness and strain tolerance. The weaker panel-level separation at high core stiffness (≈1.08-fold, against ≈2.2-fold at core level) further indicates that the panel response becomes facesheet- or shear-limited in that regime.

This work sets a straightforward precedent for connecting resin-AM lattice design parameters to sandwich panel performance in an experimentally honest, application-relevant framework. Furthermore, this research highlights the potential to develop a design toolkit to achieve mechanically engineered sandwich structures from partially biobased and low-impact constituents for lightweight structural applications.

CRediT author contributions

LL: Investigation, Writing – original draft (support); SS: Software, Writing – review & editing; MC: Investigation, Writing – review & editing; SG: Supervision, Resources, Funding, Writing – review & editing; MV: Methodology; JAD: Conceptualization, Methodology, Formal Analysis, Resources, Visualization, Supervision, Project administration, Writing – original draft (lead).

Acknowledgements

SG acknowledges that this work is based on the research project supported in part by the National Research Foundation of South Africa (Ref: TTK240506217551).

Declaration of conflicting interests

The authors declare no conflict of interest.

Data availability

Data is available from the authors on reasonable request.

Funding Declaration

This research was supported in part by the National Research Foundation of South Africa (Ref: TTK240506217551).

Ethics, Consent to Participate, and Consent to Publish

Not applicable.

References

1. A. Almesmari, N. Baghous, C. J. Ejeh, I. Barsoum, R. K. Abu Al-Rub, *Polymers,* 2023, **15,** 19.
2. A. Bustihan, I. Botiz, *Polymers,* 2026, **18,** 1019.
3. I. Roohani, A. Entezari, H. Zreiqat, *Additive Manufacturing,* 2023, **74,** 103720.
4. B. Ngatane, J. A. Dicks, W. H. Ho, M. Ngoepe, *MATEC Web of Conferences,* 2024, **406,** 07014.
5. J. A. Dicks, M. I. Hoosain, O. Mbele, *South African Journal of Industrial Engineering,* 2024, **35,** 52-65.
6. A. Temiz, *Journal of the Brazilian Society of Mechanical Sciences and Engineering,* 2024, **46,** 121.
7. F. H. Öztürk, İ. A. Karamanlı, A. Temiz, *International Journal of Mechanics and Materials in Design,* 2025, **21,** 591-608.
8. M. S. Hossain, M. M. Hossain, S. Nilufar, *Polymers,* 2025, **17,** 24.
9. S. Z. Ahmad, M. H. Masood, M. U. Khattab, S. S. Ahmad, S. A. A. Zaidi, S. Z. Khan, *Materials,* 2025, **18,** 22.
10. N. Baghous, M. A. Abraham, N. T. Mogos, R. K. Abu Al-Rub, *Scientific Reports,* 2025, **16,** 1.
11. H. Doostmohammadi, S. Khaleghi, M. Baghani, M. Karimpour, S. Bagherifard, M. Baniassadi, *Advanced Engineering Materials,* 2025, **27,** 2402679.
12. O. Al-Ketan, R. K. Abu Al-Rub, *Material Design & Processing Communications,* 2021, **3,** e205.
13. Z. Chen, P. Han, J. Liu, G. Bai, N. Xiao, Z. Xia, *Mechanics of Advanced Materials and Structures,* 2025, **32,** 125-138.
14. R. Gabrieli, R. Wenger, M. Mazza, E. Verné, F. Baino, *Materials,* 2024, **17,** 654.
15. B. Yilmaz, *Mechanics of Advanced Materials and Structures,* 2024, **31,** 3492-3502.
16. Y. Wakjira, A. Cioni, H. G. Lemu, *Progress in Additive Manufacturing,* 2025, **10,** 1085-1102.
17. Y. Wakjira, A. Cioni, H. G. Lemu, H. R. Hagland, *Journal of the Mechanical Behavior of Biomedical Materials,* 2026, **173,** 107237.
18. C. A. Ramírez Rodríguez, C. A. Narváez Tovar, D. A. Garzon-Alvarado, *SSRN,* 2024.

19. B. Huffman, G. Youssef, *Progress in Additive Manufacturing,* 2025, **10,** 10145-10157.
20. S. Kavafaki, G. Maliaris, *Engineering Proceedings,* 2025, **87,** 46.
21. A. Crill, S. Gabriel, J. A. Dicks, *MATEC Web of Conferences,* 2026.
22. G. Di Bella, M. Chairi, G. Marabello, V. Palomba, *Journal of Sandwich Structures & Materials,* 2025.
23. M. S. El-Asfoury, N. E. El-Bedwehy, M. Shazly, A. Elkaseer, *Scientific Reports,* 2026, **16**.
24. J. Justino Netto, M. Sardinha, M. Leite, *Mechanics of Materials,* 2024, **195**.
25. J. Peloquin, Y. Han, K. Gall, *Additive Manufacturing,* 2023, **78**.
26. L. Garzon, S. Ferrandiz Bou, E. Rayón Encinas, P. Abril, C. Cobos Maldonado, *Progress in Additive Manufacturing,* 2026, **11,** 8.
27. A. Pham, C. Kelly, K. Gall, *Journal of Materials Research,* 2020, **35,** 19.
28. H. S. Bharath, D. Bonthu, S. Gururaja, P. Prabhakar, M. Doddamani, *Composite Structures,* 2021, **263**.
29. S. Chahardoli, *Journal of Sandwich Structures & Materials,* 2023, **25,** 2.
30. İ. K. Türkoğlu, H. Kasım, M. Yazıcı, *International Journal of Protective Structures,* 2023, **14,** 1.
31. C. Peng, P. Tran, A. P. Mouritz, *Composite Structures,* 2022, **300,** 116167.
32. H. Junaedi, M. A. Abd El-baky, M. M. Awd Allah, T. A. Sebaey, *Polymers,* 2024, **16,** 1698.
33. S. A. M. Ghannadpour, M. Mahmoudi, K. Hossein Nedjad, *Composite Structures,* 2022, **281**.
34. K. Makarian, M. Taghvaei, J. Tu, N. J. Alvarez, G. R. Palmese, *Composite Structures,* 2023, **318**.
35. A. Vasile, D. M. Constantinescu, I. C. Coropeţchi, Ş. Sorohan, D. A. Apostol, *Solids,* 2024, **5,** 4.
36. L. Stepinac, J. Galić, A. P. Vassilopoulos, *Composite Structures,* 2024, **343**.
37. V. Patekar, K. Kale, *Polymer Composites,* 2022, **43,** 9.
38. W. C. Jang, H. D. Roh, *International Journal of Precision Engineering and Manufacturing,* 2025, **26,** 8.
39. H. Jamshaid, R. Mishra, *The Journal of The Textile Institute,* 2016, **107,** 7.
40. P. Jagadeesh, S. M. Rangappa, S. Siengchin, *Construction and Building Materials,* 2024, **436**.
41. H. H. Farghal, T. M. Madkour, *Journal of Composites Science,* 2026, **10,** 5.
42. P. F. Jacobs, *Rapid Prototyping & Manufacturing: Fundamentals of Stereolithography*. Society of Manufacturing Engineers: **1992**.
43. P. M. Bean, *On the Mechanical Properties of Additively Manufactured Gyroids*. The University of Maine: **2025**.
44. E. Bol, M. Ramulu, *Materials & Design,* 2025.
45. L. J. Gibson, M. F. Ashby, *Cellular Solids: Structure and Properties*. 2 ed.; Cambridge University Press: **1997**.
46. Y. Huang, L. Zhai, *Scientific Reports,* 2025, **15,** 1.
47. M. Abdelaal, I. Eldesouky, *Progress in Additive Manufacturing,* 2025, **10,** 10.
48. J. A. Dicks, M. I. Hoosain, O. Mbele, *South African Journal of Industrial Engineering,* 2024, **35,** 4.
49. R. Kumar, J. Ramkumar, K. Balani, *Journal of the Mechanical Behavior of Biomedical Materials,* 2026, **173**.

50. Y. Li, H. Gu, M. Pavier, H. Coules, *Proceedings of the Institution of Mechanical Engineers, Part C: Journal of Mechanical Engineering Science,* 2020, **234,** 16.
51. T. J. Kolibaba, E. T. Iverson, H. Legendre, C. I. Higgins, Z. N. Buck, T. S. Weeks, J. C. Grunlan, J. P. Killgore, *ACS Appl Mater Interfaces,* 2023, **15,** 12.
52. K. C. H. Chin, G. Ovsepyan, A. J. Boydston, *Nature Communications,* 2024, **15,** 1.
53. K. Hayashi, R. Kishida, A. Tsuchiya, K. Ishikawa, *ACS Applied Materials & Interfaces,* 2023, **15,** 29.
54. T. Dixit, E. Al-Hajri, M. C. Paul, P. Nithiarasu, S. Kumar, *Applied Thermal Engineering,* 2022, **210**.
55. E. Mancini, M. Utzeri, E. Farotti, A. Lattanzi, M. Sasso, *Mechanics of Materials,* 2024, **192**.
56. G. Colombini, M. Giacalone, F. Torri, F. Berni, S. Mantovani, S. Defanti, E. Bassoli, *Procedia CIRP,* 2025, **135**.
57. T. Maconachie, R. Tino, B. Lozanovski, M. Watson, A. Jones, C. Pandelidi, A. Alghamdi, A. Almalki, D. Downing, M. Brandt, M. Leary, *The International Journal of Advanced Manufacturing Technology,* 2020, **107,** 11-12.
58. Z. Yang, F. Lu, X. Zhan, H. Zhu, B. Zhang, Z. Chen, H. Zhang, *Journal of Building Engineering,* 2024, **84**.
59. C. Ralph, P. Lemoine, J. Summerscales, E. Archer, A. McIlhagger, *Textile Research Journal,* 2019, **89,** 15.
60. A. Zubail, A. Traidia, M. Masulli, K. Vatopoulos, T. Villette, I. Taie, *Journal of Cleaner Production,* 2021, **305**.
61. C. King, E. Van Roijen, H. Choudhary, S. A. Miller, *ACS Sustainable Chemistry & Engineering,* 2025, **13,** 30.
62. M. W. Iqbal, K. Shaker, 13 - Life-Cycle Assessment of Ballistic Vest. In *Composite Solutions for Ballistics*, Nawab, Y.; Sapuan, S. M.; Shaker, K., Eds. Woodhead Publishing: 2021; pp 341-358.
63. N. Farazmandnia, A. Ilinca, *Materials (Basel),* 2025, **18,** 16.
64. C. Chen, Y. Ding, X. Wang, L. Bao, *Polymer Composites,* 2024, **45,** 14.
65. V. Raghuvanshi, M. Singh, S. Dodla, D. Khan, *Fibers and Polymers,* 2025, **26,** 2.
66. M. Ntloane, S. Gabriel, S. Chung Kim Yuen, J. A. Dicks, *MATEC Web of Conferences,* 2026.
67. N. E. El-Bedwehy, A. Elkaseer, M. A. El-Hadek, M. Arafa, *Journal of Engineering and Applied Science,* 2025, **72,** 1.

Supplementary Files

This is a list of supplementary files associated with this preprint. Click to download.

- SImanuscript.pdf